



Numerical Analysis of the High Speed Driven Cavity Flow in 2-D Curved Channel

M. M. A. Alam^{1†}, T. Setoguchi¹, M. Takao² and H. D. Kim³

¹ Institute of Ocean Energy, Saga University, Japan

² Department of Mechanical Engineering, Matsue National College of Technology, Japan

³ Department of Mechanical Engineering, Andong National University, Korea

† Corresponding Author Email: dralam@me.saga-u.ac.jp

(Received December 2, 2014; accepted January 12, 2015)

ABSTRACT

Numerical experiments were carried out on the high speed driven cavity flows in 2D curved channels to investigate mainly the pressure field. A density-based algorithm in ANSYS Fluent 13.0 was used in the present URANS simulations. The SST $k-\omega$ model was used for modeling the turbulence within an unstructured mesh solver. Validation of the numerical code was accomplished, and the results showed a good agreement between the numerical simulation and experimental data. Three channels (straight, concave and convex) with a nominal height of $H = 4 \times 10^{-3}$ m under the transonic flow conditions were considered in the study. The cavity studied is $L = 12 \times 10^{-3}$ m long with the depth ranging from $D = 12 \times 10^{-3}$ m to 48×10^{-3} m to obtain the length-to-depth ratios of $L/D=1$ to $1/4$. The study comprised the analysis of the cavity surface pressures and the associated flow structures. The channel configuration influenced the cavity flowfield, and that influence finally resulted in a change in the surface pressure fluctuations in the cavity. The deep cavity attenuated the flowfield oscillation inside the cavity.

Keywords: Compression wave; Compressible flow; Oscillation; Pressure fluctuation; URANS (unsteady Reynolds-averaged Navier-Stokes)

NOMENCLATURE

C_p	specific heat at constant pressure	Re	Reynolds number
D	depth of the cavity	St	Strouhal number
E	total energy	t	time
f	frequency	T	temperature periodic time
h	specific enthalpy	u, v	velocity components
H	height of the channel	U_∞	free stream velocity
k	turbulent kinetic energy	μ	dynamic viscosity
L	length of the cavity	ρ	density
	characteristic length	ω	specific dissipation rate
M	Mach number	0	stagnation
p	static pressure	t	turbulent
q	heat flux		
R	radius of the curvature		

1. INTRODUCTION

The high speed driven-cavity flowfields are often characterized by the compression waves, expansion waves, shear layer and an oscillation inside the cavity. Many researches have been conducted over the past decades to inves-

tigate the external flows over the cavity (Charwat *et al.* (1961), Hahn (1969), Rockwell and Naudascher (1978), Zhang and Edward (1990)). Some researches for the internal flows around the cavity (Matsuo *et al.* (2005), Matsuo *et al.* (2007), Setoguchi *et al.* (2006)) have been conducted in relation to the supersonic air-intake

that is an essential part of the air breathing engine. The cavity plays an important role in the control of shock waves (Seddon and Goldsmith (1985)). The transonic or supersonic air-intake flow tends to be unstable due to the separations induced by the shock / boundary layer or the shock / shear layer interactions (Seddon and Goldsmith (1985), Dougherty *et al.* (1990)).

The transonic or supersonic flows over the cavity accompanying with the shear layer separation from the upstream lip, and a series of vortices travel downstream in the cavity and strikes or reattaches on the rear end with the generation of the compression waves. These compression waves then propagate upstream within the cavity and excite the shear layer at the cavity upstream. As a result, the process is sustained by completing the feedback loop as first described by Krishnamurty (1955) and later on by Rossiter (1964). The modification of the shear layer continues by the subsequent excitations, and consequently resonance occurs when the frequency and the phase of the shear layer match those of the compression waves. The resonance, thus produced, largely amplifies the cavity pressure fluctuations.

In the present study, the CFD work was conducted to investigate the high speed driven cavity flows in 2D curved channels. Three channels (straight, concave and convex) under the transonic flow conditions were considered to analyze the effect of channel configuration on the flowfield. Considering the computational cost, the unsteady RANS simulation using the SST $k-\omega$ turbulence model was conducted. The cavity surface pressure fluctuations and the associated flow structures were investigated. The numerical code used in the study was validated through the comparison with the experimental data, and with the theoretical results.

2. NUMERICAL MODEL AND COMPUTATIONAL METHODOLOGY

2.1 Governing Equations

The cavity flows in 2D curved channel were treated as compressible, viscous, unsteady and turbulent. The governing equations used are the time-dependent Navier-Stokes equations given in vector form as shown below:

$$\frac{\partial \mathbf{W}}{\partial \mathbf{Q}} \frac{\partial}{\partial t} \int_V \mathbf{Q} dV + \oint [F - G] dA = \int_V \mathbf{H} dV \quad (1)$$

where the vectors \mathbf{W} , \mathbf{Q} , \mathbf{F} , and \mathbf{G} are defined as,

$$\mathbf{W} = \begin{bmatrix} \rho \\ \rho u \\ \rho v \\ \rho E \end{bmatrix}, \quad \mathbf{Q} = \begin{bmatrix} p \\ u \\ v \\ T \end{bmatrix}, \quad \mathbf{F} = \begin{bmatrix} \rho v \\ \rho v u + p \hat{i} \\ \rho v v + p \hat{j} \\ \rho v E + p v \end{bmatrix} \quad (2)$$

and,

$$\mathbf{G} = \begin{bmatrix} 0 \\ \tau_{xi} \\ \tau_{yi} \\ \tau_{ij} v_j + q \end{bmatrix} \quad (3)$$

The vector \mathbf{H} contains the source terms of the body forces and energy sources. In the above equations, ρ , v , E , and p are the density, velocity, total energy per unit mass, and the pressure of the fluid, respectively. τ is the viscous stress tensor, and q is the heat flux. The total energy E is related to the total enthalpy H by $E = H - p/\rho$ where, $H = h + |v|^2/2$.

The Jacobian matrix $\partial \mathbf{W} / \partial \mathbf{Q}$ in Eqn. (1) is replaced with the preconditioning matrix Γ for transforming the system into the conservation form, and the matrix Γ is given by,

$$\Gamma = \begin{bmatrix} \Theta & 0 & 0 & \rho_T \\ \Theta u & \rho & 0 & \rho_T u \\ \Theta v & 0 & \rho & \rho_T v \\ \Theta H - \delta & \rho u & \rho v & \rho_T H + \rho C_p \end{bmatrix} \quad (4)$$

where,

$$\rho_T = \left. \frac{\partial \rho}{\partial T} \right|_p \quad (5)$$

and the parameter Θ is given by,

$$\Theta = \left(\frac{1}{U_r^2} - \frac{\rho_T}{\rho C_p} \right) \quad (6)$$

C_p is the specific heat at constant pressure. The reference velocity U_r is chosen locally such that the eigenvalues of the system remain well conditioned with respect to the convective and diffusive time scales (Weiss and Smith (1995)).

To close the governing equations, the $k-\omega$ SST model which is a two equation eddy-viscosity (Shear Stress Transport) turbulence model (Mentor (1993), Mentor (1994), Mentor *et al.* (2003)) was employed in the present computation. This turbulence model is an effective

blend of the robust and accurate formulation of the Wilcox's k - ω model in the near-wall region with the free-stream independence of the k - ϵ model in the far field. The turbulent kinetic energy k and the specific dissipation rate ω are determined by the following transport equations.

$$\frac{\partial}{\partial t}(\rho k) + \frac{\partial}{\partial x_i}(\rho k u_i) = \frac{\partial}{\partial x_j}(\Gamma_k \frac{\partial k}{\partial x_j}) + \tilde{G}_k - Y_k \quad (7)$$

$$\frac{\partial}{\partial t}(\rho \omega) + \frac{\partial}{\partial x_i}(\rho \omega u_i) = \frac{\partial}{\partial x_j}(\Gamma_\omega \frac{\partial \omega}{\partial x_j}) + G_\omega - Y_\omega + D_\omega \quad (8)$$

In these equations, \tilde{G}_k represents the generation of the turbulent kinetic energy due to the mean velocity gradients, G_ω represents the generation of ω , and D_ω is the cross-diffusion term. Γ_k and Γ_ω represent the effective diffusivity of k and ω , respectively. Y_k and Y_ω represent the dissipation of k and ω due to turbulence.

The effective diffusivities for the model are given by,

$$\Gamma_k = \mu + \frac{\mu_t}{\sigma_k} \quad (9)$$

$$\Gamma_\omega = \mu + \frac{\mu_t}{\sigma_\omega} \quad (10)$$

where, σ_k and σ_ω are the turbulent Prandtl numbers for k and ω , respectively, and they are given by;

$$\sigma_k = \frac{1}{F_1/\sigma_{k,1} + (1-F_1)/\sigma_{k,2}} \quad (11)$$

and

$$\sigma_\omega = \frac{1}{F_1/\sigma_{\omega,1} + (1-F_1)/\sigma_{\omega,2}} \quad (12)$$

The turbulent viscosity μ_t is computed as;

$$\mu_t = \frac{\rho k}{\omega} \frac{1}{\max[1/\alpha^*, SF_2/a_1/\omega]} \quad (13)$$

where S is the strain rate magnitude, defined as;

$$S \equiv \sqrt{2S_{ij}S_{ij}} \quad (14)$$

and

$$S_{ij} = \frac{1}{2} \left(\frac{\partial u_j}{\partial x_i} + \frac{\partial u_i}{\partial x_j} \right) \quad (15)$$

The coefficient α^* damps the turbulent viscosity causing a low-Reynolds-number correction. It is given by,

$$\alpha^* = \alpha_\infty^* \left(\frac{\alpha_0^* + \text{Re}_t/R_k}{1 + \text{Re}_t/R_k} \right) \quad (16)$$

where,

$$\text{Re}_t = \frac{\rho k}{\mu \omega} \quad (17)$$

The blending functions F_1 and F_2 are given by,

$$F_1 = \tanh(\Phi_1^4) \quad (18)$$

$$\Phi_1 = \min \left[\max \left(\frac{\sqrt{k}}{0.09\omega y}, \frac{500\mu}{\rho y^2 \omega} \right), \frac{4\rho k}{\sigma_{\omega,2} D_\omega^+ y^2} \right] \quad (19)$$

$$D_\omega^+ = \max \left[2\rho \frac{1}{\sigma_{\omega,2}} \frac{1}{\omega} \frac{\partial k}{\partial x_j} \frac{\partial \omega}{\partial x_j}, 10^{-10} \right] \quad (20)$$

and,

$$F_2 = \tanh(\Phi_2^2) \quad (21)$$

$$\Phi_2 = \max \left[2 \frac{\sqrt{k}}{0.09\omega y}, \frac{500\mu}{\rho y^2 \omega} \right] \quad (22)$$

where, y is the distance to the next surface and D_ω^+ is the positive portion of the cross-diffusion term.

The cross-diffusion term D_ω is defined as;

$$D_\omega = 2(1-F_1)\rho\sigma_{\omega,2} \frac{1}{\omega} \frac{\partial k}{\partial x_j} \frac{\partial \omega}{\partial x_j} \quad (23)$$

Model constants are given as;

$$\sigma_{k,1} = 1.176, \sigma_{\omega,1} = 2.0, \sigma_{k,2} = 1.0, \sigma_{\omega,2} = 1.168$$

$$a_1 = 0.31, \alpha_\infty = 0.52, \alpha^* = \alpha_\infty^* = 1.0, \alpha_0^* = \beta_i/3$$

$$\beta_i = 0.072, R_k = 6$$

2.2 Numerical Methods

The density-based algorithm in ANSYS Fluent 13.0 (ANSYS (2013)) was used to solve the governing equations. A fully implicit method was implemented on the present spatial domain. The convective fluxes were formulated using the Roe's flux difference splitting scheme (Roe

(1981)). The 3rd order accuracy was conceived from the original MUSCL (van Leer (1979)) finite volume scheme that is a blend of central differencing and second-order upwind schemes, in which the physical domain is subdivided into numerical cells, and the integral equations were applied to each cell. Second-order central difference scheme was used for viscous terms. For the time derivatives, an implicit multistage time stepping scheme was used.

2.3 Computational Conditions

Cavity flows in 2D curved channel simulated and the geometric detail of the channel and cavity are shown in Fig. 1. Three channel configurations, straight channel, concave channel and convex channel, were used in the present computational work. The nominal height of the channel is $H=4$ mm, and the radius of curvature of the curved channel is $R=80$ mm. The rectangular cavity depth was changed between $D=12$ mm and 48mm, and the length was kept constant at $L=12$ mm. The computational area was meshed with structural mesh elements using ICEM 13.0. The typical mesh used is shown in Fig. 1(d). The grids were densely clustered in the boundary / shear layers and in the cavity in order to provide more reasonable predictions. The fineness of the computational grids was examined through the several tests to ensure that the obtained solutions were independent of the grids employed. The cavity flow in the straight channel were considered for the mesh dependency test. The surface pressure fluctuations at locations 1, 2, 3, 4 and 5 in the 12 mm deep cavity as indicated in Fig. 1(a) were recored, and the amplitude of the pressure fluctuations were compared for the 5 (five) different meshes. The detailed information about these 5 (five) different meshes are presented in Table 1. Figure 2 shows the predicted surface pressure fluctuations during the 4 ms of time at the location 3 (as shown in Fig. 1(a)) for mesh type 2, 3, and 4. Here, the pressure samples were taken in the random manner. The discrepancy between the amplitudes is found reducing with the grid refinement. Moreover, both the type 3 and 4 meshes were captured the surface pressure fluctuations almost with the same resolution. Considering the computational cost, hence, the type 3 mesh in which the number of grids is 200×50 in the channel and 100×90 in the cavity was used in the present simulation.

The subsonic incoming flow having free stream Mach and Reynolds numbers of $M=0.76$ and $Re=50,400$, respectively, flows over the rectangular cavity. Flow passed the cavity become

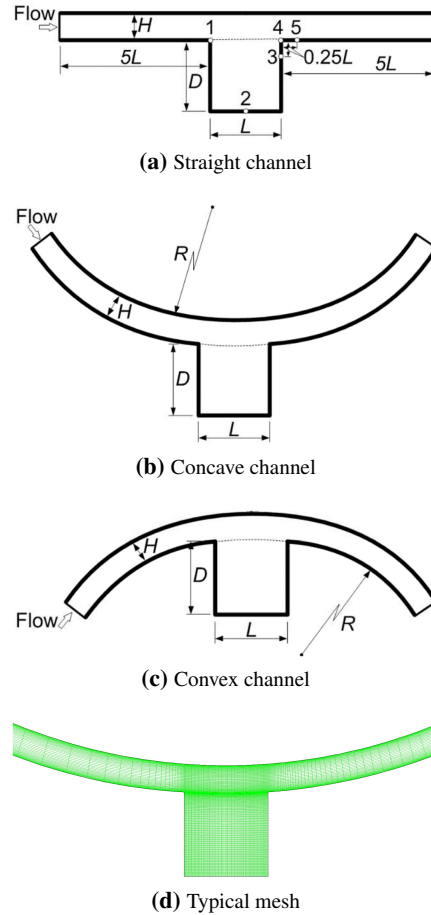


Fig. 1. Schematics of the computational domain and the typical mesh.

Table 1 The detail of the different meshes

Mesh type	Number of grids	
	channel	cavity
1	160×30	80×70
2	180×40	90×80
3	200×50	100×90
4	200×60	100×100
5	210×60	110×100

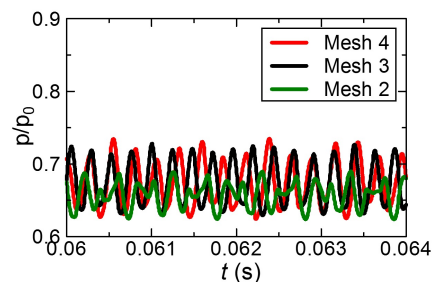


Fig. 2. Comparison of the surface pressure fluctuations for the different meshes.

transonic. The inlet total pressure and temperature were $p_0=101.3$ kPa and $T_0=293$ K, respectively. The boundary conditions used were the inlet total pressure and the outlet static pressure at the upstream and downstream of the com-

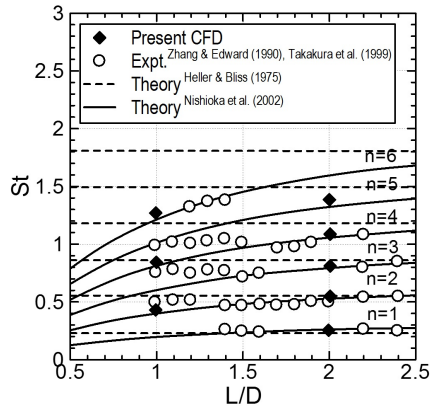


Fig. 3. Strouhal numbers as a function L/D .

putational domain, respectively. Adiabatic and no-slip boundary conditions were applied to the solid wall surfaces.

A solution convergence was obtained when the residuals for each of the conserved variables were reduced below the order of magnitude 6. Another convergence criterion was to check the conserved quantities directly through the computational boundaries. The net mass flux was investigated when there was an applicable imbalance through the computational boundaries.

3. RESULTS AND DISCUSSION

To validate the computational code developed for the present numerical simulations, the supersonic flow (inlet Mach number $M_{inlet} = 1.83$) over the 2D open cavities of length to depth ratios L/D of 1.0 and 2.0 was investigated and the predicted results were compared with the experimental and theoretical results (Heller and Bliss (1975), Zhang and Edward (1990), Nishioka *et al.* (2002), Takakura *et al.* (1999)). Figure 3 shows the comparison of the Strouhal numbers St . The abscissa and ordinate in the figure denote the cavity length to depth ratio, L/D and the Strouhal number, St (normalized frequency: fL/U_∞), respectively. The solid and broken lines are obtained from the formulae of predicting oscillation frequencies proposed by Nishioka *et al.* (2002) and by Heller and Bliss (1975), respectively. The open circle represents the experimental results reported by Zhang and Edward (1990) and by Takakura *et al.* (1999). The closed diamond represents the predicted results from the present simulation. The comparison shows that the predicted results have a good agreement with the experimental data (Zhang and Edward (1990), Takakura *et al.* (1999)) and with the theoretical results (Heller and Bliss (1975), Nishioka *et al.* (2002)).

Figure 4 shows density contour sequences dur-

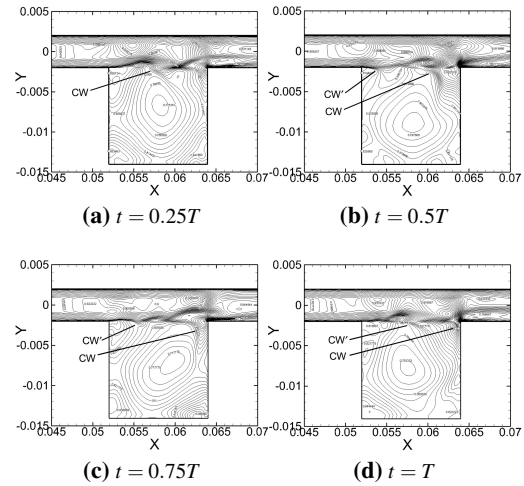
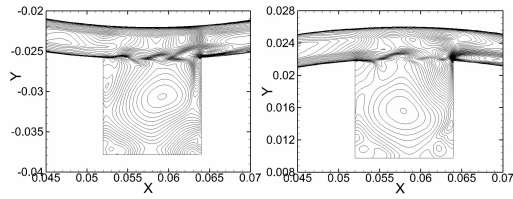


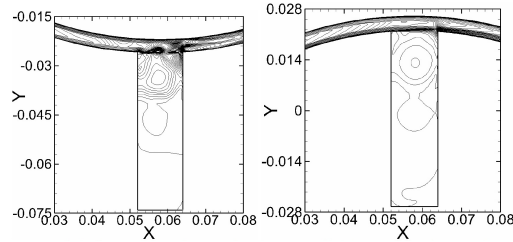
Fig. 4. Iso-density contours of the cavity flow in the straight channel ($D=12$ mm).

ing one periodic time (T) of flow field oscillation for the cavity flows in straight channel. It was observed that a compression wave (CW) from the trailing edge of the cavity moves upstream. The upstream compression waves propagate toward the cavity leading edge and disturb the shear layer. This disturbance regenerates instability waves in the shear layer. While the shear layer reattaches at the rear wall of the cavity, generation of compression waves occurs due to the impingement of instability waves on the wall. These compression waves propagate upstream within the cavity and further disturb the shear layer. The shear layer is continuously modified due to these subsequent disturbances and finally resonance occurs when frequency and the phase of the waves match with those of the shear layer instability waves. While the shear layer for cavity flow in concave channel, as shown in the instantaneous density contour in Fig. 5(a), tends to be directed downward and strikes on the aft of the cavity trailing edge, and finally resulting in the increase of the static pressure inside the cavity compared with the straight and convex channels. In the cavity flow through convex channel, the shear layer tries to elevate slightly from the cavity, and thus strikes at the corner of the cavity trailing edge, as shown in Fig. 5(b). The oscillation for this case is quite similar to the cavity flow in the straight channel.

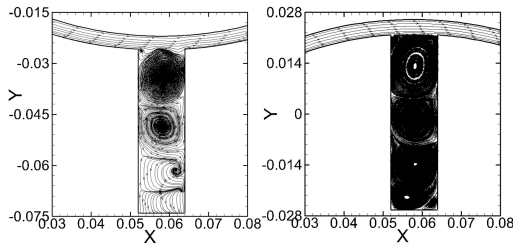
Figure 6 shows the instantaneous density contours of the cavity flow in the concave and convex channels. When the cavity depth increases to $D=48$ mm, some vortical structures along the depth can be found inside the cavity. The flow entrainment effect leads to the generation of these consecutive vortical struc-



(a) Concave channel (b) Convex channel
Fig. 5. Instantaneous iso-density contours of $D=12$ mm cavity flow.



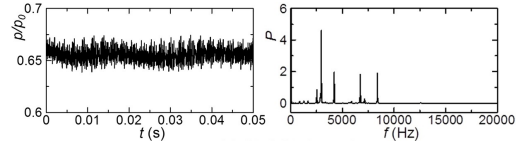
(a) Concave channel (b) Convex channel
Fig. 6. Instantaneous iso-density contours of $D=48$ mm cavity flow.



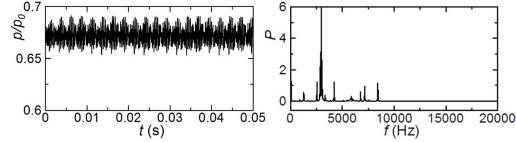
(a) Concave channel (b) Convex channel
Fig. 7. Instantaneous contours of the streamlines of $D=48$ mm cavity flow.

tures, and they can clearly be visualized from the streamline contours those are shown in Fig. 7. This phenomenon results in the decrease of the dynamic pressures that accompanying with the increase in the static pressure in the cavity. The relatively high static pressure weakens the strength of the compression waves that are generated from the trailing edge and as well as the shear layer disturbance, and finally, resulting in the reduction of the pressure fluctuations in the cavity, as shown in Fig. 6(a). For the cavity flow in the convex channel in Fig. 6(b), it can be found almost an oscillation free flowfield.

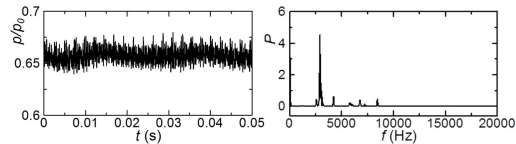
To get a quantitative picture of the flowfield oscillation, pressures were measured at five different locations (location 1, 2, 3, 4 and 5) as indicated in Fig. 1(a). The power spectra of pressure fluctuations with time at these five locations were evaluated using the FFT (Fast Fourier Transform) analysis. The time histories of static pressure and power spectra of pressure



(a) Straight channel



(b) Concave channel



(c) Convex channel

Fig. 8. Time history and power spectra of the pressure fluctuations at the cavity bottom ($D=12$ mm).

fluctuations at cavity bottom (point 2) for $D=12$ mm and 48 mm deep cavities are presented in Figs. 8 and 9, respectively. For $D=12$ mm deep cavity, the pressure fluctuates, as shown in Fig. 8, with time around a frequency of 2.9 kHz. The average pressure at cavity bottom is maximum for the cavity flow in the concave channel, as shown in Fig. 8(b). The peak of power spectra is relatively higher for the cavity flow in the concave channel. It indicates that the energy of turbulent fluctuations that leads to the fluctuations in the pressure field is higher for the concave channel than that of other cases. On the contrary, for $D=48$ mm deep cavities, the pressure fluctuates with time at much smaller amplitude, as shown in Fig. 9, than that of the $D=12$ mm deep cavities. From Fig. 9(c), the cavity flow in the convex channel exhibits almost an oscillation free pressure at the cavity bottom (point 2).

4. CONCLUSION

The present numerical work was performed to investigate the effect of the channel configurations on the high speed driven cavity flows. The time dependent Reynolds averaged Navier-Stokes (RANS) equations with the SST $k-\omega$ turbulence model were used to analyze the problem. The concave channel was found to influence the cavity flows. The static pressures inside the cavity and the surface pressure fluctuations were found higher in the concave channel in comparison with the straight and convex channels. The deep cavities accompanied with the vortical structures along

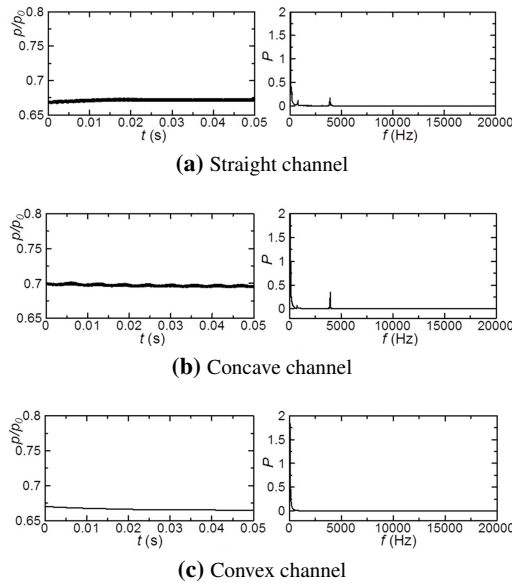


Fig. 9. Time history and power spectra of the pressure fluctuations at the cavity bottom ($D=48$ mm).

the cavity depth reducing the surface pressure fluctuations.

REFERENCES

- ANSYS (2013). *Fluent Users guide*. USA.
- Charwat, A., J. Ross, F. Dewey and J. Hitz (1961). An investigation of separated flows - part i: The pressure field. *Journal of Aerospace Science* 28(6), 457–470.
- Dougherty, N., J. Hot, T. Nesman and R. Farr (1990). Time accurate navier-stokes computation of self-excited two-dimensional unsteady cavity flows. *AIAA Paper 90-0691*.
- Hahn, M. (1969). Experimental investigation of separated flow over a cavity at hypersonic speed. *AIAA Journal* 7(6), 1092–1098.
- Heller, H. and D. Bliss (1975). The physical mechanism of flow-induced pressure fluctuations in cavities and concepts for their suppression. *AIAA Paper 75-491*.
- Krishnamurty, K. (1955, August). Acoustic radiation from two dimensional rectangular cutouts in aerodynamic surfaces. Technical Note 3487, NACA.
- Matsuo, S., M. Alam, T. Nakano, M. Tanaka, T. Setoguchi and K. Kaneko (2005, October 12–15). Effect of non-equilibrium condensation of moist air on supersonic cavity flow. In *Proceedings of the 8th Asian International Fluid Machinery Conference*, Yichang, China.
- Matsuo, S., M. Alam, T. Setoguchi, H. Kim and S. Yu (2007, July 2–5). A new passive method of controlling cavity-induced pressure oscillations. In *Proceedings of the 8th International Symposium on Experimental and Computational Aerothermodynamics of Internal Flows*, Ecole Centrale de Lyon, France.
- Mentor, F. (1993). Zonal two equation $k - \omega$ turbulence models for aerodynamic flows. *AIAA Paper 93-2906*.
- Mentor, F. (1994). Two equation eddy-viscosity turbulence models for engineering applications. *AIAA Journal* 32, 269–289.
- Mentor, F., M. Kuntz and R. Langtry (2003). Ten years of industrial experience with the sst turbulence model. In K. Hanjalic, Y. Nagano and M. Tummers (Eds.), *Turbulence, Heat and Mass Transfer*, Number 4, pp. 625–632. Begell House Inc., USA.
- Nishioka, M., T. Asai, S. Sakaue and K. Shiraji (2002). Some thoughts on the mechanism of supersonic cavity flow oscillation, part 2: A new formula for the oscillation frequency. *Journal of the Japan Society of Fluid Mechanics* 21, 368–378.
- Rockwell, D. and E. Naudascher (1978). Review - self-sustaining oscillations of flow past cavities. *Journal of Fluids Engineering* 100, 152–165.
- Roe, P. (1981). Approximate riemann solvers, parameter vectors and difference schemes. *Journal of Computational Physics* 43, 357–372.
- Rossiter, J. (1964, October). Wind tunnel experiments on the flow over rectangular cavities at subsonic and transonic speeds. Reports and Memoranda 3438, Aeronautical Research Council.
- Seddon, J. and E. Goldsmith (1985). *Intake Aerodynamics*. AIAA Education Series.
- Setoguchi, T., M. Alam, S. Matsuo, K. Teramoto and S. Yu (2006). A numerical study on passive control of cavity induced pressure fluctuations in two-dimensional supersonic flow. *International Journal of Turbo and Jet Engines* 23(3), 155–164.
- Takakura, Y., T. Suzuki, F. Higashino and M. Yoshida (1999, January 11-14). Numerical study on supersonic internal cavity flows: What causes the pressure fluctuations? In *Proceedings of the 37th*

AIAA Aerospace Science Meeting and Exhibition, Reno, NV.

van Leer, B. (1979). Towards the ultimate conservative difference scheme v: A second order sequel to godunov's method. *Journal of Computational Physics* 32, 101–136.

Weiss, J. and W. Smith (1995). Precondition-

ing applied to variable and constant density flows. *AIAA Journal* 33(11), 2050–2057.

Zhang, X. and J. Edward (1990). An investigation of supersonic oscillatory cavity flows driven by thick shear layers. *Aeronautical Journal* 94, 355–364.